Engineering Structures 335 (2025) 120335

Contents lists available at ScienceDirect

Engineering Structures

journal homepage: www.elsevier.com/locate/engstruct

A refined DS-InSAR technique for long-term deformation monitoring of low-coherence bridge groups

Yun Zhou [a,b,c], Guanwang Hao [b,*], Xiaoqiong Qin [d], Fan Yi [b], Zhongkun Tan [e]

[a] Key Laboratory for Damage Diagnosis of Engineering Structures of Hunan Province, Hunan University, Changsha 410082, China
[b] College of Civil Engineering, Hunan University, Changsha 410082, China
[c] Key Laboratory of Building Safety and Energy Efficiency of the Ministry of Education, Hunan University, Changsha 410082, China
[d] State Key Laboratory of Intelligent Geotechnics and Tunnelling, Shenzhen University, Shenzhen 518060, China
[e] Zhongteng Zhixin Technology (Hunan) Co., Ltd., Changsha, China

ARTICLE INFO

Keywords:
Long-span bridge
Interferometric synthetic aperture radar (InSAR)
Structural health monitoring
Distributed scatterer interferometry
Bridge deformation

ABSTRACT

Satellite-based Interferometric Synthetic Aperture Radar (InSAR) is a radar technique capable of detecting millimeter-scale deformations in long-span bridges. However, many InSAR methods estimate thermal dilation phase using air temperature data from nearby airports rather than the bridge site, neglecting spatial variations in temperature distribution. Moreover, InSAR measurements are typically referenced to a high-coherence point, which assumes stable scattering characteristics over time but fails to consider the structural features of bridges. To address these issues, this paper develops a refined Distributed Scatterer InSAR (RDSI) technique, focusing on thermal dilation phase estimation and reference point selection for phase unwrapping. First, the local thin-plate spline method was employed to estimate bridge site temperature using longitude and latitude as independent variables and elevation as a covariate. Then, a structural-knowledge-driven reference point selection method was developed by installing artificial radar corner reflectors (CRs) at the fixed bearing and identifying their echo signals in SAR imagery. The RDSI technique was applied to three different types of long-span bridges, including a continuous arch bridge, a suspension bridge, and a cable-stayed bridge. Using 20 COSMO-SkyMed images collected from 2022 to 2024, the line-of-sight (LOS) displacement was obtained. The correlation between LOS deformation and air temperature of different bridge structures was analyzed. To validate the precision of the RDSI technique, LOS cumulative deformations were inverted using BeiDou Navigation Satellite System (BDS) measurements of vertical, north-south, and west-east displacements. The comparison between BDS-based and RDSI-based LOS cumulative deformations revealed that the bridge movement direction captured by RDSI aligns well with BDS measurements, with a maximum error of 1.18 mm. This suggests that RDSI is a promising technique for the safety monitoring of urban bridge groups.

1. Introduction

Structural health monitoring (SHM) of long-span bridges is essential for infrastructure safety. Currently, bridge deformation assessment primarily relies on periodic manual inspections, including visual inspection, total station surveys, leveling, microwave radar, photogrammetry, laser scanning, and digital image processing, as well as sensor-based monitoring using displacement meters, inclinometers, connecting tubes, and global navigation satellite systems. These techniques are suitable for evaluating critical individual bridges. However, deploying them to monitor 1079,300 bridges in China is cumbersome even impractical, especially given limited financial resources.

1.1. Synthetic aperture radar (SAR) interferometry (InSAR)

InSAR is a cost-effective remote monitoring technique that can measure deformation covering large geographical areas and various weather conditions utilizing the interferometric phase between two echoes of the same observed target. It has been widely applied in the infrastructure deformation monitoring, including highways [1], buildings [2,3], railways and subways [4], transportation networks [5], dams [6], slopes [7], airports [8], etc. The Persistent Scatterer Interferometry

* Corresponding author.
E-mail addresses: zhouyun05@hnu.edu.cn (Y. Zhou), gwh0114@hnu.edu.cn (G. Hao), xqqin@szu.edu.cn (X. Qin), yifance@hnu.edu.cn (F. Yi), tzktzk9888@hnuedu.cn (Z. Tan).

https://doi.org/10.1016/j.engstruct.2025.120335
Received 23 December 2024; Received in revised form 1 April 2025; Accepted 12 April 2025
Available online 18 April 2025

(PSI) approach, by focusing on stable points from a sequence of SAR images, addresses problems such as atmospheric delays, temporal decorrelation, and spatial decorrelation, enabling effective monitoring of small movements. The PSI technique was employed by Huang et al. [9] to monitor the displacement of a high-speed railway bridge, the results highlight a significant relationship between deformation and air temperature at the time of image acquisition. A single-track stack of COSMO-SkyMed (CSK) and multi-track stacks of Sentinel-1A (S1A) data, processed utilizing the PSI technique, indicate that the thermal dilation is the primary contributor to bridge displacements [10]. Cusson et al. [11] applied PSI with thermal sensitivity to detect millimeter-level motion on two steel truss bridges and establish early warning thresholds for bridge movements. Ma et al. [12] developed a geometry-based InSAR network to monitor the deformation of the Hong Kong-Zhuhai-Macao Bridge (HZMB), followed by an analysis of the influence of multiple environmental factors. Zhou et al. [13] developed a PSI technique incorporating the structure's temperature field for long-span bridge deformation monitoring, revealing a strong spatio-temporal relationship between displacement and air temperature. Farneti et al. [14] proposed a multidisciplinary approach combining InSAR with numerical modeling to monitor bridge displacements, predict failure times, and assess structural collapse due to slow deformation phenomena. Guzman-Acevedo et al. [15] integrated InSAR time-series data with a calibrated finite element model to assess bridge safety, estimating risk based on service, fracture, and statistical displacement thresholds. For bridges with low backscattering capability, SAR faces challenges in detecting adequate persistent scatterer (PS) to characterize detailed spatial deformation. Qin et al. [16,17] analyzed the SAR incoherent information and foreground-background scattering of bridges, which led to a 40 % increase in the density of extracted point-like targets. Based on the Gaussian Mixture Model-Expectation Maximization algorithm, the density and quality of PS points on the under-construction cross-sea bridge was enhanced [18]. TerraSAR-X radar imagery in the Staring SpotLight mode from both ascending and descending orbits was processed using the SqueeSAR, resulting in a high density of measurement points [19]. However, enhancing PS point density with multi-source SAR data is unsuitable for widespread application due to limited SAR coverage for some bridges. On the other hand, employing high-resolution SAR images for InSAR monitoring will inevitably increase costs. Therefore, the Distributed Scatterer InSAR (DSI) technique was developed for surface motion monitoring at low-coherence regions, where adjacent pixels exhibit similar reflectivity and similar statistical properties [20–22]. Nevertheless, few studies have investigated the capability of the DSI technique in detecting bridge deformations [23].

1.2. Reference point (RP) selection for phase unwrapping

To obtain accurate deformation measurements, phase unwrapping is required by adding the correct wrap count to each pixel. Using an RP selected by the coherence-based method as the starting point, the absolute phase in the interferogram is recovered through path integration of the estimated phase gradient. The coherence-based method selects RPs from stable scattering regions with high coherence, which are assumed to undergo negligible deformation. Traditional phase unwrapping methods fall into two categories: path-following [24], which selects an integration path to prevent local errors from spreading, and optimization-based [25], which minimizes the difference between the estimated and unwrapped phase gradients to achieve optimal results. Moreover, a method that combines traditional phase unwrapping techniques with deep learning is proposed to overcome the complex wrapped phase caused by topographic features and the low coherence coefficient [26,27]. The aforementioned studies obtained the line of sight (LOS) displacement relative to an RP but overlooked the impact of RP movement on InSAR deformation analysis. However, if the RP experiences unnoticed movements, the LOS displacements of other scatterers will be inaccurately estimated. To accurately interpret InSAR rates as uplift or subsidence, a well-defined Earth-centered terrestrial reference framework is established through continuously operating reference stations of the Global Navigation Satellite System (GNSS) [28]. The optimal RP was automatically selected for InSAR time series analysis, considering the temporal coherence and phase connectivity between each RP and the target wetland [29]. Based on InSAR and GNSS measurements, the absolute InSAR estimation was obtained by rigidly attaching phase-stable millimeter-precision compact active radar transponders to GNSS antennas [30]. The combination of GNSS and InSAR observations can be used to derive absolute LOS deformation measurements [31]. However, its application is limited by labor and financial costs.

1.3. Thermal dilation estimation

In previous research on the thermal dilation estimation, air temperature measured at a nearby airport was typically used to represent the temperature of bridge sites, so the spatial variation of ambient air temperature was often ignored. Generally, the bridge temperature distribution is investigated by combining numerical simulation and field measurements [32]. Using field meteorological measurements, the time-dependent thermal boundary conditions can be determined and then applied to a two-dimensional fine finite-element model of typical sections of the box girder for the transient heat-transfer analysis [33,34]. To improve the efficiency and accuracy of the temperature distribution of the entire bridge, Xia et al. [35,36] then conducted a three-dimensional heat-transfer analysis, in which the measured air temperature and solar radiation were used as the thermal boundary conditions. It is evident that collecting extensive temperature data through the field monitoring system is crucial for accurately determining the temperature distribution of bridges. However, bridge temperature fields analysis via field sensors or detailed simulations demands high manpower and material costs. For bridges lacking field measurements, the boundary conditions for thermal analysis are typically determined using meteorological data from a nearby airport [37]. Based on ambient temperature data sourced from a meteorological data sharing platform, an inverse square distance gradient method was adopted to calculate the air temperature of bridges [13]. Thermal analysis for bridges without using field measurements is applicable to InSAR technique for bridge deformation monitoring.

1.4. Accuracy assessment of InSAR deformation measurements

The precision of InSAR technique in deformation monitoring has been validated by comparisons of displacements between InSAR-derived results and alternative measurement techniques, such as classical geodetic surveying, field sensors monitoring, and computer simulations. Lorenz et al. [38] tested the thermal deformation of a curved highway bridge utilizing InSAR technique and compared the results with geodetic data and simulations of the longitudinal displacements over the observation period. The differential PSI deformation has been used as inputs to calculate stress using a finite element model, and the results are consistent with the recorded damage information [39]. By installing corner reflectors (CRs) on bridges, the InSAR-measured longitudinal displacement was compared with data obtained from automated total stations to assess the measurement accuracy of InSAR [40]. A controlled experiment was conducted using CRs to evaluate the capabilities of InSAR in determining vertical displacements of bridges, and the discrepancy compared to leveling measurements is less than 2 mm [41]. The PSI-derived bridge deformation was decomposed into longitudinal deformation and compared with the measurements from field sensors and simulations, and the relative error was within 5 % [13]. InSAR measures one-dimensional LOS deformation, requiring decomposition into horizontal or vertical components for accuracy assessment. However, the non-target directional displacements need to be neglected, leading to potential overestimation of target deformation.

To the best of the authors' knowledge, few studies have concerned the influence of coherence-based RP selection on InSAR deformation measurements. Additionally, the spatial variations in air temperature distribution are often neglected in thermal dilation estimation. Therefore, a refined DSI (RDSI) is developed through structure-driven RP selection and air temperature interpolation at bridge sites, enhancing the accuracy of phase unwrapping and thermal dilation estimation, respectively. Specifically, an artificial radar CR was installed at the bridge's fixed bearing, and corresponding signal was identified as the RP in the SAR intensity image for phase unwrapping, eliminating errors from manual RP selection. Next, air temperature at the bridge site for thermal dilation estimation was derived using a local thin-plate spline based on ground weather station data, accounting for the effect of elevation on spatial distribution of air temperature. Finally, the precision of RDSI was validated by introducing the concept of LOS cumulative displacement and comparing InSAR-derived deformations with BeiDou regional navigation satellite system (BDS) measurements on the bridge deck.

2. Methodology

2.1. RDSI technique

A single resolution unit (pixel) of SAR images contains multiple sub-scatterers. Ground targets can be divided into persistent scatterer (PS), distributed scatterer (DS), and incoherent scatterers according to their backscatter characteristics and stability. Assuming N SAR images are available for the observation area over a specific period, one image can be chosen as the master image, while the other images using as slave images [42]. The slave images are co-registered with the master image, and *N-1* interferometric pairs are generated. Differential interferometric processing, based on digital elevation models (DEM), is performed on these pairs to produce differential phases as follows [43]:

$$\psi = \varphi_{\mathrm{ref}} + \varphi_{\mathrm{top}} + \varphi_{\mathrm{def}} + \varphi_{\mathrm{atm}} + \varphi_{\mathrm{noi}} \tag{1}$$

where, the interferometric phase in SAR images is influenced by several errors, which can be categorized into five components: φ_{ref} denotes orbit estimation errors, φ_{top} is the elevation errors, φ_{def} signifies the LOS deformation, φ_{atm} represents the atmospheric phase delay, and φ_{noi} accounts for the noise and other error components.

Air temperature plays a crucial role in the long-term deformation of long-span bridges. To address this, the RDSI technique integrates thermal dilation parameters into the interferometric model's nonlinear deformation component, as represented by the following equation:

$$\psi = \frac{4\pi}{\lambda} t\cdot v + \frac{4\pi}{\lambda R \sin\theta} B\cdot\varepsilon + \frac{4\pi}{\lambda} T\cdot k + \varphi_{\mathrm{res}} \tag{2}$$

where λ denotes the radar wavelength, R represents the slant range, θ indicates the radar incidence angle, B refers to the vertical baseline, ε accounts for the DEM elevation error, t represents the temporal baseline, v is the linear deformation velocity, T stands for the air temperature at the bridge site during each image acquisition, k is the thermal dilation coefficient, and φ_{res} represents the residual phase, including atmospheric phase, nonlinear deformation components, and noise. To mitigate cloud-induced atmospheric delay effects on the reliability of InSAR measurements, the atmospheric phase is separated from the residual phase by filtering, leveraging its characteristics of low spatial frequency and high temporal frequency.

The workflow of RDSI technique, which is depicted in Fig. 1, involves four steps: pre-processing, DS processing, PS processing, and deformation results generation.

Step 1: Pre-processing. From a set of SAR images, the master image is chosen based on the minimal temporal and spatial baselines. All slave images are aligned to the master using the coherence coefficient method.

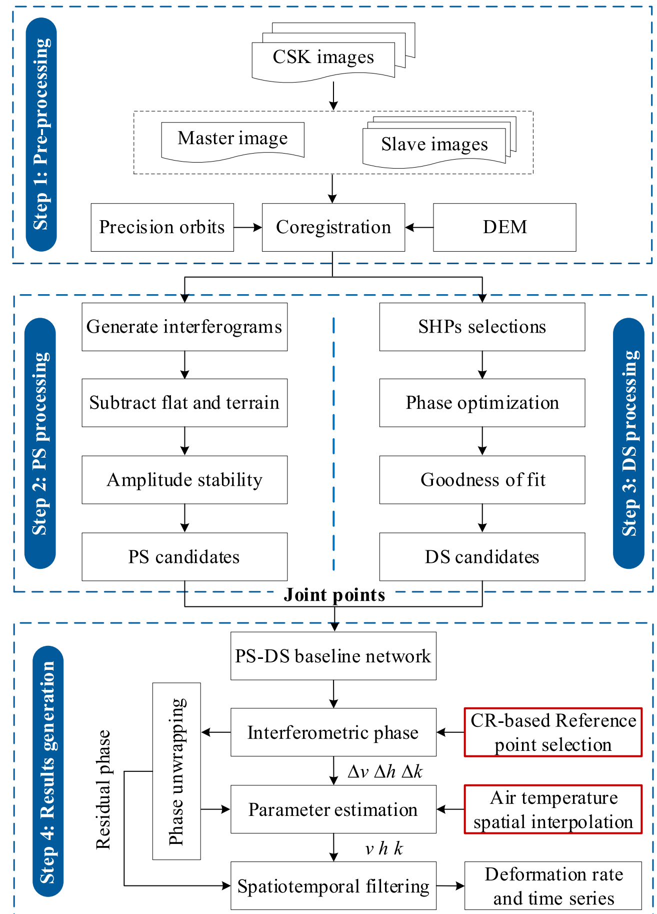

Fig. 1. RDSI processing flow.

With precise orbit and DEM data, the SAR images are registered and clipped, resulting in differential interferogram pair sequences.

Step 2: PS processing. The amplitude threshold and amplitude dispersion index are both employed to select PS points, with high-amplitude pixels chosen as candidates and those with smaller amplitude deviations selected as final PS points. Consequently, the selected PS points exhibit stable radar scattering characteristics, which enhance the accuracy of InSAR deformation calculations.

Step 3: DS processing. The selection of DS points involves statistical homogeneous pixels (SHPs) identification and phase optimization. SHPs are determined based on the intensity of SAR images, which is then utilized to refine the interferometric phase. Temporal coherence is employed to assess the effectiveness of phase optimization, and the "goodness of fit" index is utilized to assess the quality of phase estimation for selecting high-quality DS points.

Step 4: Deformation results generation. An artificial radar CR is installed at the fixed bearing of a bridge, and its corresponding signal is identified as a RP for phase unwrapping. The phases of combined coherent points are differentiated, unwrapped, and triangulated to separate linear deformation, elevation residuals, and residual phases. The thermal dilation phase is estimated by interpolating air temperature at the bridge site using measured data form the ground weather station. Singular value decomposition then yields the deformation velocity and cumulative deformation over the study period.

2.2. Air temperature calculation for bridge sites

Based on the air temperature from ground weather stations and the elevation of the study area, the air temperature at bridge sites is interpolated utilizing the local thin plate spline [44]. This method incorporates the elevation as a covariate for comprehensive statistical analysis, balancing the smoothness of the interpolation surface with its accuracy. Essentially, it generalizes standard multiple linear regression by replacing the parameter model with a smooth non-parametric function. The degree of smoothing is automatically determined from the data using generalized cross-validation (GCV) or generalized maximum likelihood (GML) [45]. The theoretical statistical model can be expressed as follows:

$$Z_i = f(x_i) + \mathbf{b}^{\mathrm{T}}\mathbf{y}_i + e_i \quad (i = 1, 2, \cdots, N) \tag{3}$$

where Z_i represents the value to be estimated at point i in space, $f(x_i)$ is an unknown smooth function of the variable to be estimated, b is the ρ-dimensional coefficient of $\mathbf{y}_i$, $\mathbf{y}_i$ is a ρ-dimensional vector of independent auxiliary variables, e_i denotes the random error of the variable x_i to be estimated, with an expected value of 0, and N is the number of known sites. The unknown smooth function $f(x_i)$ is estimated using the least squares method:

$$\min\left[\sum_{i=1}^{N}\left(\frac{e_i}{w_i}\right)^2 + \rho J_m(f)\right] \tag{4}$$

where $J_m(f)$ represent the roughness measure function of $f(x_i)$, defined as the m-th partial derivative of $f(x_i)$. w_i refers to the variance of the relative error, and ρ denotes the smoothing parameter that balances data fidelity and surface roughness. Typically, ρ is determined by minimizing GCV and GML [46]. The fitting function for the vector is as follows:

$$\widehat{Z} = AZ \tag{5}$$

where A indicates an N-dimensional influence matrix.

$$GCV = \frac{\left\|W^{-1}(I-A)Z\right\|^2 / N}{[trace(I-A)/N]^2} \tag{6}$$

$$W = diag(w_1 \ldots w_n) \tag{7}$$

where W is a diagonal matrix and trace (I-A) represents the degrees of freedom.

The flowchart of air temperature calculation using local thin plate spline is illustrated in Fig. 2. SPLINA/B is suitable for thin plate spline analysis with independent variables or multiple covariates. The inputs include the observed values from the weather station, along with its longitude, latitude, and elevation information. In addition to calculating air temperature, the outputs also contain the standard deviation of the observed data evaluating the quality of the interpolation, as well as the GCV and GML criteria for selecting the best model.

2.3. RP identification for phase unwrapping driven by structural knowledge

The interferometric phase is wrapped within (−π, π] due to trigonometric functions in the transmitting and receiving models [47]. To avoid error transfer in the phase unwrapping process caused by coherence-based RP selection, a RP identification method driven by structural characteristics was proposed. Normally, reaction forces and the corresponding movements follow a dual principle: a non-zero bearing force corresponds to zero movement, and vice versa. For a bridge fixed bearing, all translational degrees of freedom (longitudinal and transverse) are fixed, while rotational degrees of freedom are allowed [48]. By installing a CR at the fixed bearing on the bridge deck, the corresponding echo signal can be identified in the SAR intensity image and then used as the RP for phase unwrapping. However, pixels of the CR cannot be directly identified since SAR images typically include tremendous numbers of displayed pixels. Therefore, it is essential to convert geographical coordinates into their corresponding coordinates on the SAR intensity image. Normally, reaction forces and the corresponding movements follow a dual principle: a non-zero bearing force corresponds to zero movement, and vice versa.

Supposing the image coordinate of a CR is (I_{row}, I_{col}) and its geographical coordinate is (C_{lat}, C_{lon}), the geographical coordinate L in the same projection can be expressed as follows:

$$L = BX \tag{8}$$

$$X = \begin{bmatrix} a_1 & a_2 \\ b_1 & b_2 \\ c_1 & c_2 \end{bmatrix} \tag{9}$$

$$B = [\,I_{row} \quad I_{col} \quad 1\,] \tag{10}$$

where B represents the matrix of image coordinates, and X is the transformation coefficient matrix. If the CRs installed on the bridge are at similar elevations, the L can be rewritten as:

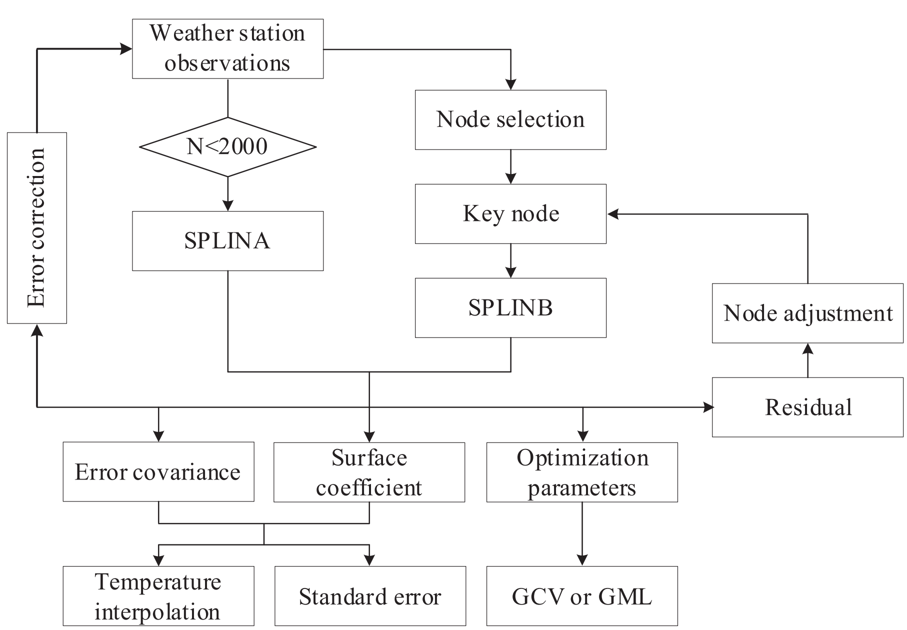

Fig. 2. Spatial interpolation flowchart.

$$L = \begin{bmatrix} I_{row} & I_{col} \end{bmatrix} \begin{bmatrix} a_1 & a_2 \\ b_1 & b_2 \end{bmatrix} \tag{11}$$

If sufficient CRs are available, least squares estimation is required to determine the conversion coefficients for data analysis.

$$L = BX + \Delta \tag{12}$$

where Δ is the observation error vector, and the least squares estimate of the conversion coefficient is given by:

$$\hat{X} = (B^T PB)^{-1} B^T PL \tag{13}$$

$$P = D_{\Delta}{}^{-1} \tag{14}$$

where P is the variance of vector Δ. The conversion parameters are used to transform the geographical coordinates of the bright spots formed by the CRs into image coordinates.

2.4. LOS cumulative displacement analysis

The LOS deformation is defined as the projection of the bridge's three-dimensional displacement onto the LOS direction. Fig. 3 illustrates the SAR side-looking imaging geometry [13]:

$$D_{\mathrm{LOS}} = D_{\mathrm{v}} \cdot \cos\theta + D_{\mathrm{n}} \cdot \sin\theta \cdot \sin\alpha - D_{\mathrm{e}} \cdot \sin\theta \cdot \cos\alpha \tag{15}$$

where D_{v}, D_{n}, D_{e} represent the displacements in the vertical, north-south, and west-east directions, respectively, θ denotes the side-looking incidence angle, and α refers to the heading angle. Accounting for bridge orientation and the spatial geometric relationship in SAR imaging, it can be expressed as follows:

$$D_{\mathrm{LOS}} = D_{\mathrm{v}} \cdot \cos\theta - D_{\mathrm{n}} \cdot \sin\theta \cdot \sin(\alpha+\beta) - D_{\mathrm{e}} \cdot \sin\theta \cdot \cos(\alpha+\beta) \tag{16}$$

where β stands for the angle between the bridge and the true north. The relationship between the longitudinal displacement (D_l), transverse displacement (D_t), and the north-south and west-east displacements can be expressed as follows:

$$D_l = D_n \cdot \sin\beta + D_e \cdot \cos\beta \tag{17}$$

$$D_t = D_n \cdot \cos\beta - D_e \cdot \sin\beta \tag{18}$$

2.5. Method assessment metrics

To assess the performance of the air temperature interpolation model, mean relative error (MRE), root mean square error (RMSE), and mean absolute error (MAE) are presented as available quantitative performance metrics. These metrics can be represented as:

$$\mathrm{MAE} = \frac{1}{n}\sum_{i=1}^{n} |y_i' - y_i| \tag{19}$$

$$\mathrm{RMSE} = \sqrt{\frac{1}{n}\sum_{i=1}^{n} (y_i' - y_i)^2} \tag{20}$$

$$\mathrm{MRE} = \frac{1}{n}\sum_{i=1}^{n} \left| \frac{y_i - y_i'}{y_i} \right| \tag{21}$$

where y_i represents the measurements at the i-th location, and $y_i{}'$ denotes the forecast or reconstruction at the i-th location.

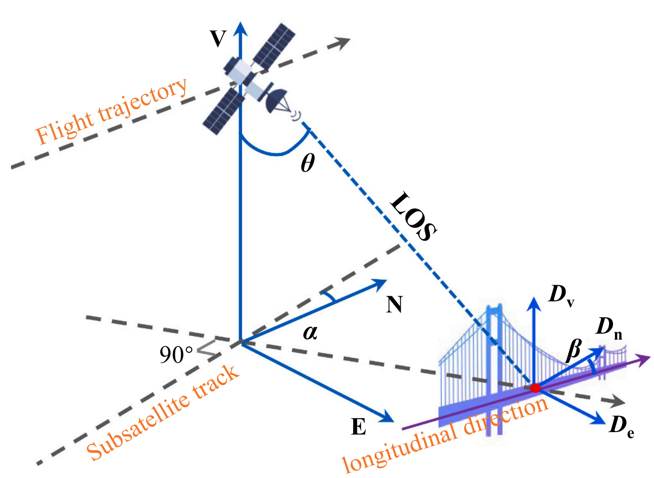

Fig. 3. SAR observation geometry of the target point.

3. Study area and data stacks

3.1. Overview of the bridge group

The bridge group across the Xiangjiang River in northern Changsha consists of three long-span bridges: a concrete cable-stayed bridge (Yinpenling Bridge, YPL), a continuous arch bridge (Fuyuanlu Bridge, FYL), and a suspension bridge (Sanchaji Bridge, SCJ). Their geographical locations are presented in Fig. 4. The longitudinal axis of SCJ is oriented at 31° relative to true north, while FYL and YPL are aligned 9° and 12° relative to true east, respectively. It is worth-noting that the nearest ground weather station, located at Huanghua International Airport, is over 25.73 km away from the case study bridges in a straight line.

3.2. SAR datasets

A total of 20 scenes of CSK stripmap imagery with a resolution of 3 m × 3 m (ascending orbit) from September 2022 to May 2024 were used. The temporal and spatial baselines of the images are shown in Fig. 5. The image captured on July 12, 2023 was selected as the main image, while the remaining images were used as slave images. The CSK satellite operates with a 24.31° incidence angle, denoted as θ, and a 168.76° heading angle, denoted as α. The radar polarization mode is HH, with a wavelength of 0.0312 m. The CSK images were captured at 22:07, so the corresponding SAR image time is approximately 6:00 (day +1) because the bridge is located in the UTC+ 8 time zone.

3.3. Meteorological data source

The studied bridge group situates in a city with complex terrain, featuring elevations ranging from −16 m to 1596 m, as illustrated in Fig. 6. Therefore, it is necessary to consider the influence of elevation on air temperature at bridge sites. This study utilized hourly air temperature measurements from September 2022 to May 2024 at the moment of SAR imaging for thermal dilation estimation in InSAR analysis, obtained from a meteorological big data platform (https://xihe-energy.com). Due to the limited number of weather stations in the studied area, the interpolation range was extended beyond the actual studied area, covering 25 sites within and around it. The 50-meter spatial resolution DEM utilized in this study was sourced from the Geographic Spatial Data Cloud (https://www.gscloud.cn/).

3.4. SAR radar CR

The artificial radar CRs are triangular in design and composed of metallic materials exhibiting high conductivity, magnetic permeability, and a substantial dielectric constant. These CRs generate strong echo signals and appear as star-shaped bright spots in SAR images, facilitating their distinctions from the background terrain. To avoid the uncertainty of phase unwrapping caused by manual selection of RPs, a total of 27

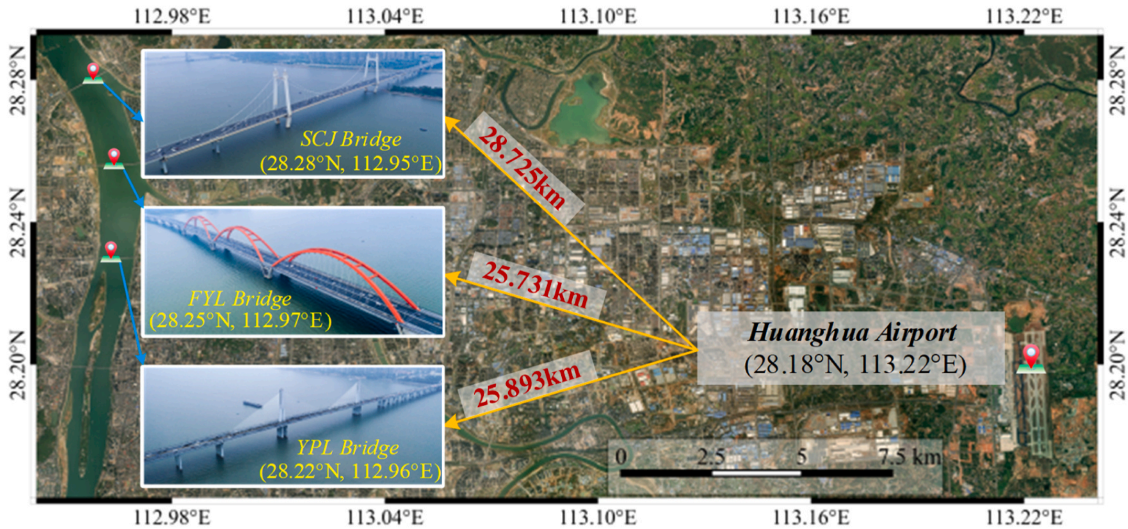

Fig. 4. Case study bridge distribution (Image by Guanwang Hao).

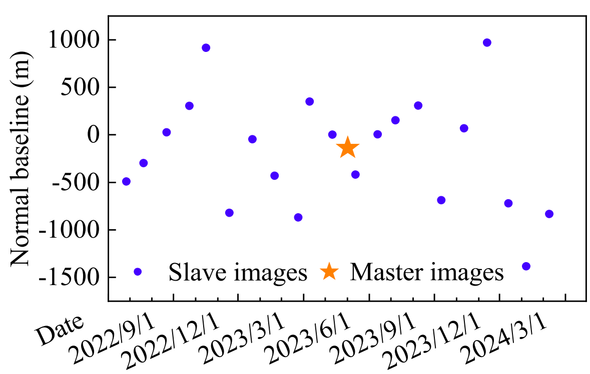

Fig. 5. Perpendicular baseline vs temporal baseline plot.

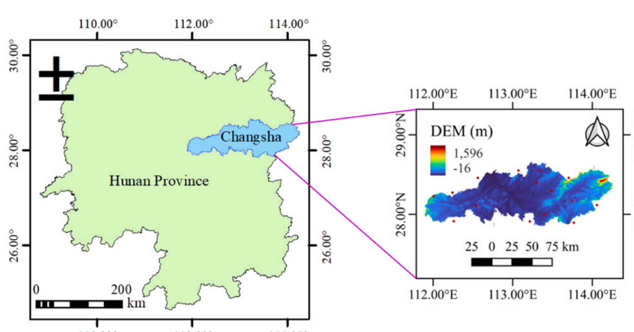

Fig. 6. Distribution of meteorological stations.

CRs were installed on the FYL Bridge as an example, including 2 clamp-type CRs mounted on the guardrail and 25 platform-type CRs on the bridge deck, as depicted in Fig. 7. One platform-type CR, specifically located at the fixed bearing on the bridge deck, was identified as the RP in the SAR intensity image for phase unwrapping.

4. Deflection of the bridge group for case study

4.1. Case study 1: FYL Bridge

4.1.1. Calculation and validation of air temperature at bridge site

The optimal spatial interpolation model for air temperature was

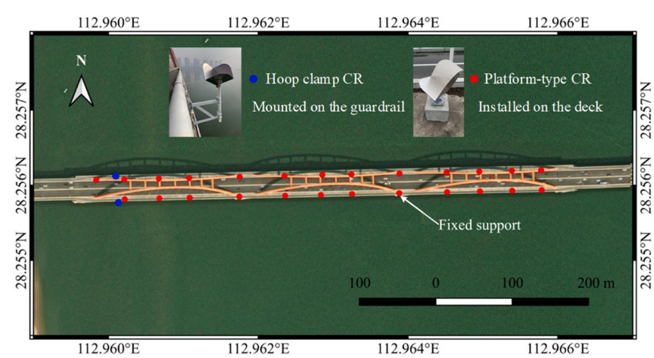

Fig. 7. RCs arrangement on FYL Bridge.

defined as a three-variable cubic spline, with longitude and latitude as independent variables and elevation as a covariate. The interpolated hourly air temperature for December 1, 2023 is shown in Fig. 8. It can be observed that air temperature and elevation are strongly correlated, with the northeastern region showing significantly lower temperatures than the central region. To verify the accuracy of the proposed interpolation method, six locations at different elevations (Datuopu DTP, Xingsha XS, Yutan YT, Huaminglou HML, Huanghua Airport HHA, and Sanchaji SCJ) were selected and compared with measured temperatures. As illustrated in Fig. 9, the results show that the MAE at each location was less than 0.7°C, with a maximum MRE of 7.74 %. Using the interpolated air temperature at bridge sites instead of weather station measurements, the thermal dilation phase estimation can be effectively improved.

To evaluate the accuracy of the RDSI technique in thermal dilation rate calculation, a comparison was conducted between the theoretical values and RDSI-derived results. The box girders of the FYL Bridge are made of Q345 steel, which has a thermal dilation coefficient k of 1.40×10^{-5} (1/°C) [49]. Taking the fixed bearing as the RP, the thermal dilation rate at different longitudinal position of the bridge can be calculated using the following equation:

$$\Delta c_{\mathrm{Long}} = \frac{\lambda}{4\pi} \cdot \Delta T \cdot k \cdot \Delta L \tag{22}$$

where λ denotes the radar wavelength, k represents the coefficient of thermal dilation, ΔT is the temperature variation, and ΔL indicates the longitudinal position. The thermal dilation rate is measured by InSAR along the LOS direction Δc_{LOS}, whereas the theoretical calculation

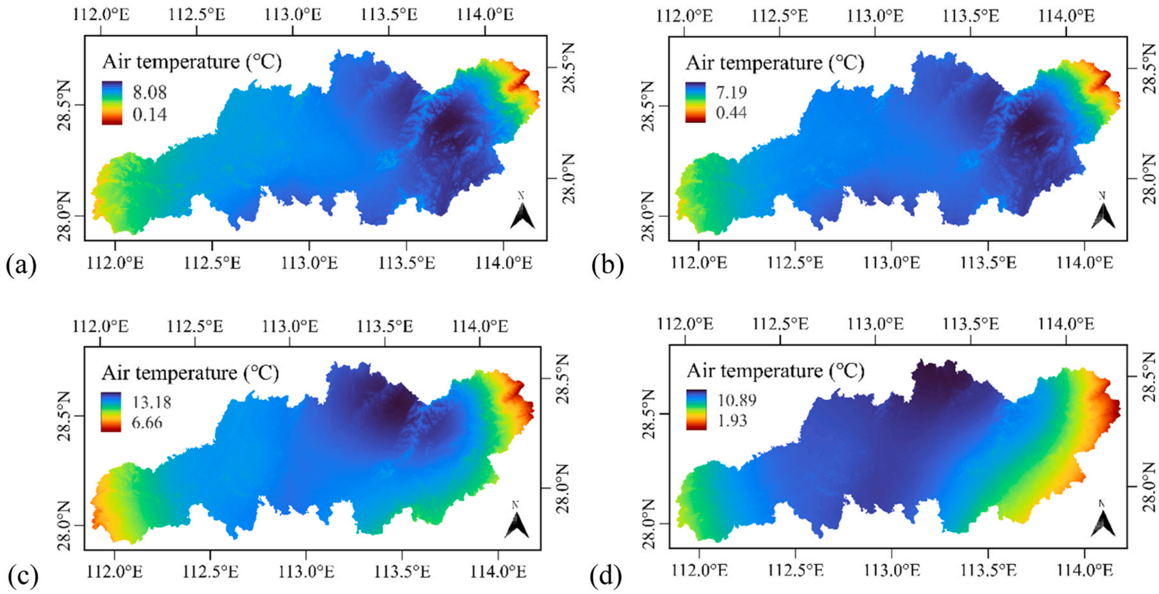

Fig. 8. Air temperature interpolation results: (a) 00:00, (b) 06:00, (c) 12:00, (d) 18:00.

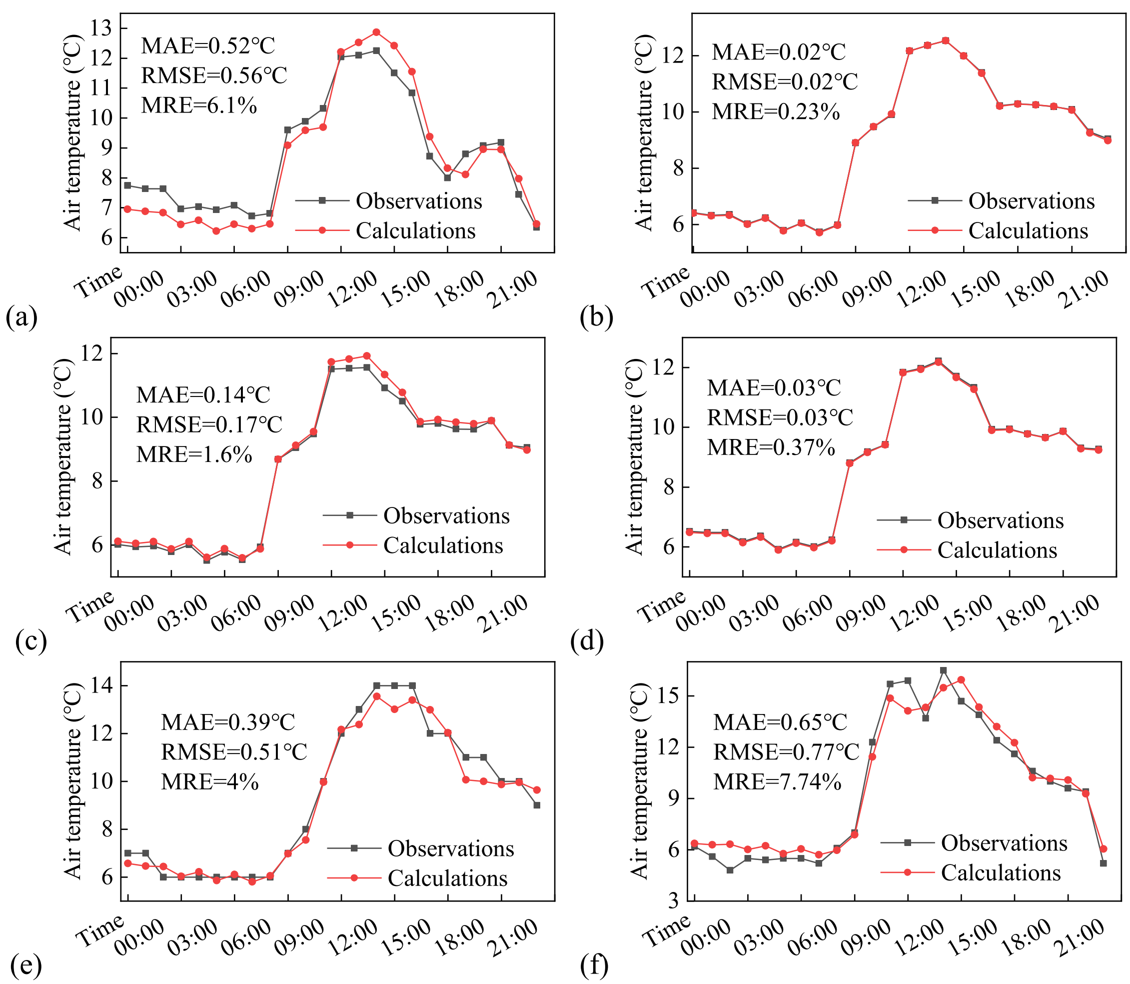

Fig. 9. Interpolation results at different positions: (a) DTP, (b) XS, (c) YT, (d) HML, (e) HHA, (f) SCJ.

provides the corresponding value in the longitudinal direction Δc_{Long}. For arch bridges with deep pile foundations, temperature-induced vertical deformation is typically limited due to high structural stiffness. For instance, Zhao et al. [50] reported that when air temperature does not exceed 30°C, the maximum vertical girder displacement of an arch bridge remains below 10 mm, indicating that this displacement can be disregarded. In addition, the thermal dilation in the transverse direction is also negligible, given that the deck width is minimal compared to the bridge's length [51]. Thus, the relationship between the Δc_{Long} and Δc_{LOS} can be expressed as follows:

$$\Delta c_{\text{LOS}} = \Delta c_{\text{Long}} \cdot \sin\theta \cdot \cos(\alpha + \beta) \tag{23}$$

The calculated and RDSI-measured thermal expansion rates are listed in Table 1. The discrepancy between the theoretical calculations and the InSAR-derived values remains within 0.1 mm/°C at all longitudinal positions, except at $\Delta L = 420$ m, where the error ranges from 3.8 % to 13.33 %. These results confirm that the thermal dilation estimated by RDSI is reliable for bridge deformation monitoring.

4.1.2. RP identification for phase unwrapping

Although CRs possess higher reflectivity, distinguishing them from terrain reflection signals in SAR images remains challenging, especially in high-resolution images, as illustrated in Fig. 10(b). To accurately identify the signals reflected by the CRs, the SAR intensity image was enhanced using the Minimum-Maximum (MinMax) stretch method, which utilizes the minimum and maximum pixel values as endpoints on the histogram to improve brightness and contrast, as presented in Fig. 10 (a). Given the latitude and longitude of the CRs installed on the bridge deck and guardrail, their geographic coordinates can be determined. The image coordinates (row, column) of the pixel points corresponding to the CRs in the MinMax-stretched SAR intensity image were computed using Eq. (8). The pixel identified from the echo signal of the CR installed at the fixed bearing was selected as the RP for InSAR phase unwrapping, as shown in Fig. 10(b).

4.1.3. Results of LOS deformation

The thermal dilation rate of the FYL Bridge is presented in Fig. 11. A sufficient number of DS and PS points were identified on the main bridge using the RDSI technique, effectively capturing the bridge's detailed deformation characteristics. In contrast, fewer scatterers were detected on the approach bridge due to the absence of arch structures, which serve as strong reflectors on the main bridge. The main bridge exhibits an increasing thermal dilation rate from the structure-driven RP to the expansion joints per unit temperature change. Specifically, the thermal dilation rate reaches −4 mm/°C at the western expansion joint and 2 mm/°C at the eastern expansion joint, compared to a range of −1–1 mm/°C at the RP. As shown in Fig. 12, the non-thermal displacement velocity map was obtained from temperature-compensated data. No significant deformation trend is observed, indicating that the bridge remained relatively stable throughout the SAR observation period.

The deformation of the bridge at the time of SAR satellite imaging is presented in Fig. 13. The temperature difference (ΔT) represents the variation in air temperature between the acquisition of the slave images and the master image. It is clear that as ΔT increases, the deformation shifts significantly from the RP toward the expansion joints. On January 16, 2023, when ΔT reached its peak of 29°C, the deformation at the west and east expansion joints of the main bridge were 100 mm and −60 mm, respectively. However, on August 13, 2023, when ΔT dropped to its minimum of 3°C, corresponding deformations were reduced to 15 mm and −10 mm, respectively.

Table 1
Calculation results of thermal dilation rate.

Δc_{LOS} (mm/°C)	ΔL= 420 m	ΔL= 315 m	ΔL= 210 m	ΔL= 105 m	ΔL= 0 m
Calculated	2.34	1.77	1.18	0.59	0
Measured	2.70	1.84	1.12	0.67	0.03
Error	13.33 %	3.80 %	5.36 %	11.94 %	-

Note: Error $= |C_i - M_i|/M_i$, where C_i represents the calculated value and M_i stands for the RDSI-measured value.

4.1.4. Comparison of DSI and RDSI results

To analyze the effect of RP selection on InSAR-measured bridge deformation, thermal dilation rates were examined using the DSI technique. The results during the SAR acquisition period are shown in Fig. 14. For DSI, an RP (marked by blue crosses) was selected was selected off the bridge from the SAR intensity image using the coherence-based method. Its physical stability was assumed based on empirical knowledge, as it was located on embankments at the riverbank, which are generally considered stable regions. However, the RP selected using the coherence-based method resulted in unreasonable DSI-derived deformations in three aspects. First, the fixed bearing of the main bridge exhibited a thermal dilation rate of 1–1.5 mm/°C and a deformation velocity of 5–10 mm/year, contradicting the expected displacement behavior. Given the constraints imposed by the fixed bearing on longitudinal, lateral, and vertical movements, this location should remain stationary. Second, the movement directions at the expansion joints of the main bridge should be opposite rather than identical. Third, the approach bridge displayed a uniform movement direction on both sides of the fixed bearing, which is structurally implausible. These findings underscore the critical role of RP selection and highlight the necessity of a refined RP identification method that incorporates the structural characteristics of bridges.

The layout of the FYL Bridge is shown in Fig. 15, where red dots indicate points A, B, and C. Their spatiotemporal deformation (RP-A, RP-B, and RP-C) was obtained using an RP at the fixed bearing, as presented in Fig. 16. Temporally, the bridge deformation exhibits a distinct periodic trend in response to temperature variations. Spatially, the strong correlations between LOS deformation and air temperature are observed at different locations. Specifically, a positive correlation is evident at point A, whereas points A and B display an opposite correlation.

To examine the sensitivity of RP selection on RDSI-measured deformation, three additional points (A, B, and C) on the bridge deck were chosen as RPs for individual InSAR analysis. The LOS deformation results, shown in Fig. 16, exhibit clear periodicity but also reveal inconsistencies with expected structural behavior. The notation RPX-Y denotes an RP at location X, where Y represents the specific point of interest. Since point B is farther from the fixed bearing than point C, its cumulative deformation should be greater. However, when point A is selected as the RP, the deformation at point B (RPA-B) is significantly smaller than that at point C (RPA-C). Similarly, selecting point C as the RP results in RPC-A and RPC-B exhibiting exaggerated deformation compared to RP-A and RP-B, due to the opposite movement direction. The results indicate that RPs located closer to the fixed bridge bearings exhibit deformation patterns that show a stronger correlation with structural characteristics.

4.2. Case study 2: SCJ bridge

The layout of the SCJ Bridge is displayed in Fig. 17, and the LOS deformation at points A, B, and C is illustrated in Fig. 18. The deformation at different locations on the bridge is strongly positively correlated with air temperature. Compared to point B, the deformation at points A and C is more sensitive to temperature changes. An RP, marked by blue crosses in Fig. 19, was selected using the proposed RP identification method. Based on this RP, the thermal dilation rate of the SCJ Bridge was analyzed, revealing a symmetrical distribution of LOS deformation about the midspan. The thermal dilation rate at the midspan and expansion joints is higher, reaching 1.5 mm/°C, while it is lower and less than 0.5 mm/°C at the bridge tower. Owing to the thermal dilation of the main cable and bridge tower, the bridge deck of the suspension bridge tends to experience downward displacement as the temperature rises. Fig. 20 demonstrates the deformation velocity of the SCJ Bridge during the SAR observation period, in which the spatial distribution aligns with that of the thermal dilation. Comparing the FYL

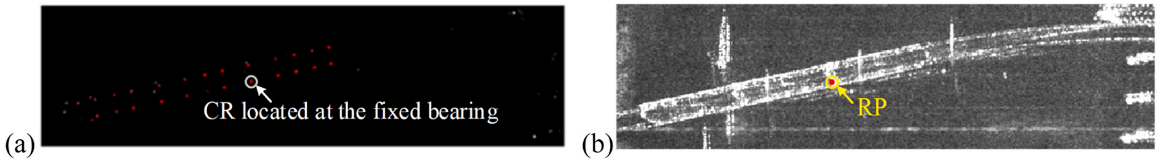

Fig. 10. RP identification results: (a) CRs' echo signals, (b) SAR intensity image.

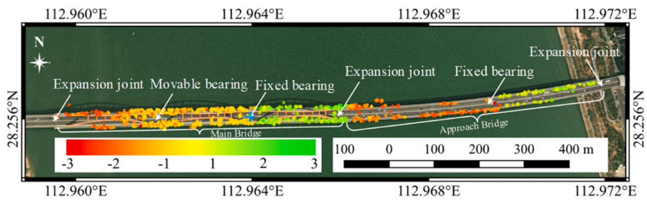

Fig. 11. LOS thermal dilation rate (mm/℃).

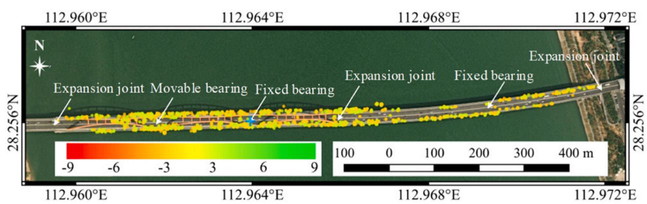

Fig. 12. LOS deformation velocity (mm/year).

Bridge with SCJ Bridge, it can be observed that the deformation velocities of different bridge types (arch bridges vs. suspension bridges) are distinguished by differences in structural forms and bearing constraints.

The air temperature at the SCJ Bridge site during SAR satellite imaging was obtained from sensors installed on the bridge deck, a nearby weather station, and an interpolation method. As depicted in Fig. 21, the interpolated temperatures align more closely with the sensor data than with the weather station records. On December 11, 2023, the weather station recorded 4°C, while the sensor measured 8.5°C, and the interpolation result was 7°C. The temperature discrepancy between the weather station and the sensor reached 4.5°C, exceeding the error between the interpolation result and the sensor data (1.5°C). Moreover, over the observation period from December 11, 2023, to May 10, 2024, the recorded temperature differences were 18°C at the weather station, 11.7°C based on sensor measurements, and 12.9°C from the interpolation method. The deviations in temperature differences between the interpolation results and the sensor data, as well as between the weather station and sensor measurements, were 1.2°C and 6.3°C, respectively. These findings demonstrate that the spatial interpolation method can provide relatively accurate air temperature measurements at the bridge site.

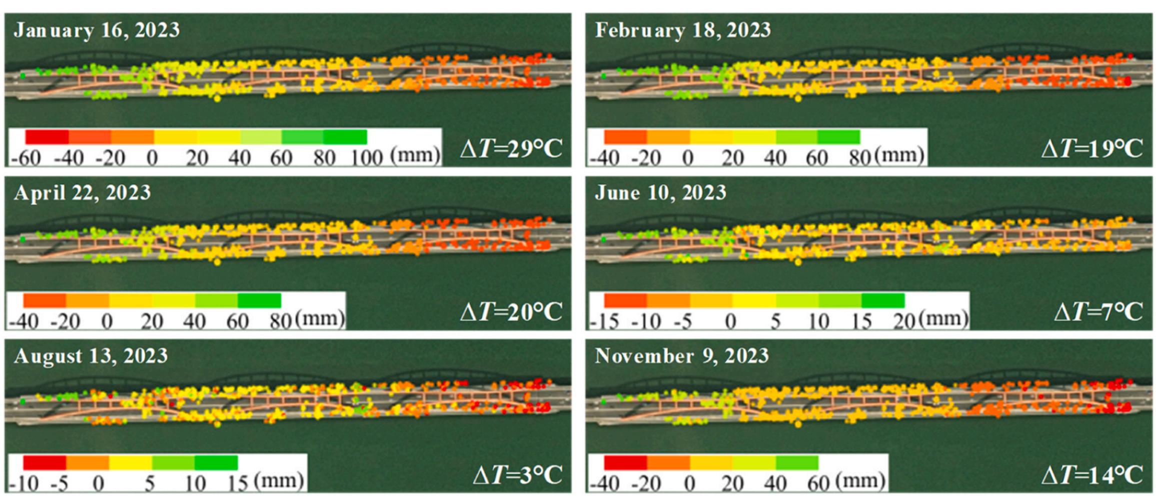

Fig. 13. LOS deformation of FYL Bridge.

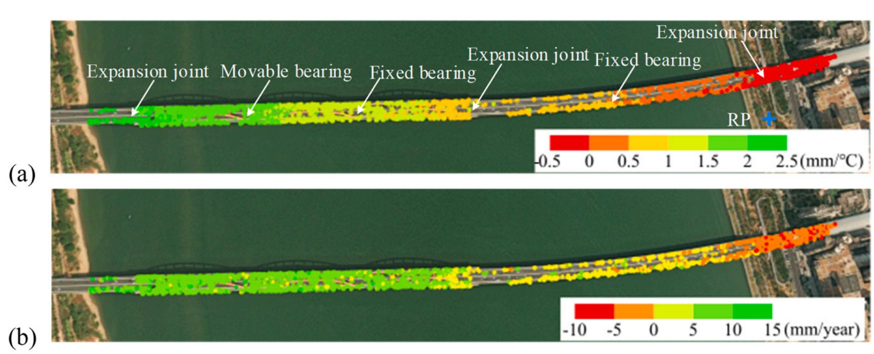

Fig. 14. Coherence-based RP identification driven DSI measurement: (a) LOS thermal dilation rate, (b) LOS deformation velocity.

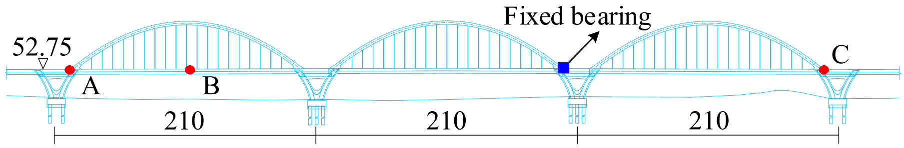

Fig. 15. Layout of the FYL bridge (unit: m).

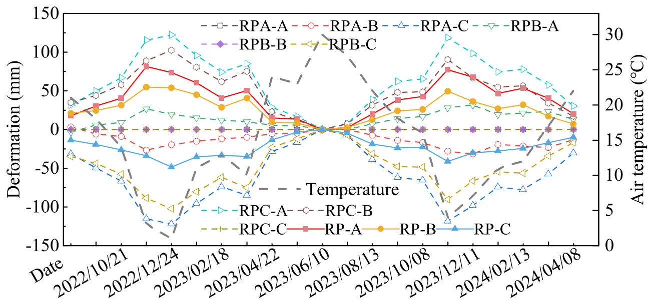

Fig. 16. RDSI deformation measurements for different RPs.

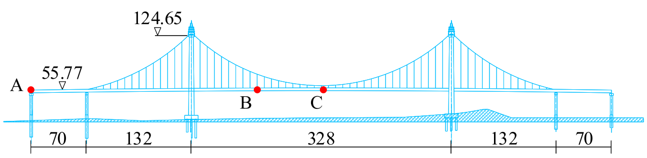

Fig. 17. Layout of the SCJ Bridge (Unit:m).

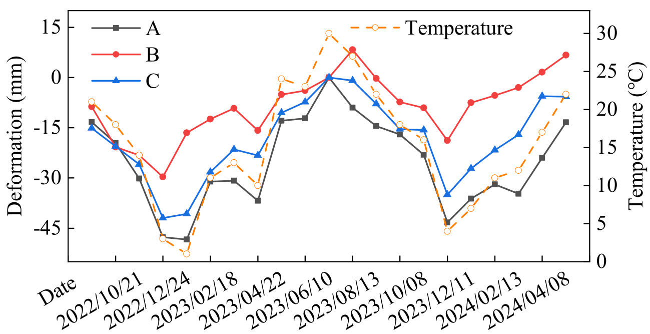

Fig. 18. Time-series LOS deformation of key point.

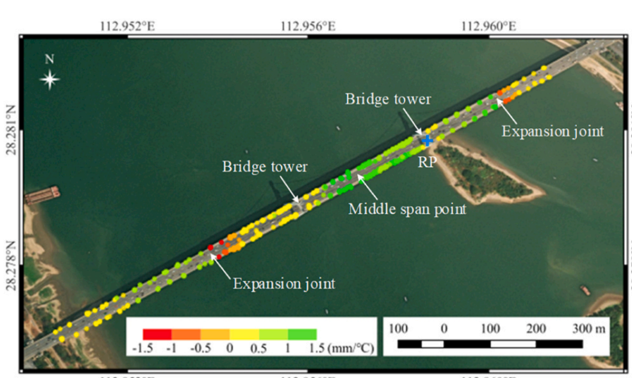

Fig. 19. LOS thermal dilation rate.

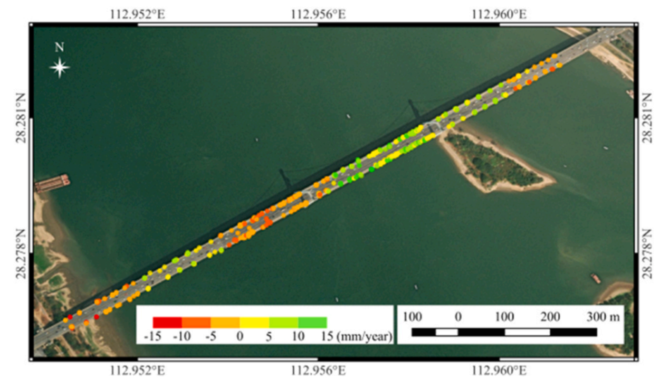

Fig. 20. LOS deformation velocity.

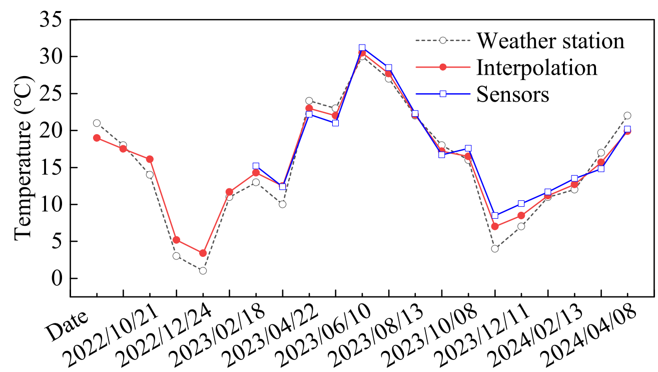

Fig. 21. Comparison of air temperature: weather station, sensor, and interpolation results.

4.3. *Case study 3: YPL bridge*

The layout of the YPL main bridge is depicted in Fig. 22. Fig. 23 presents the LOS deformation at points A and B, demonstrating a positive correlation between the deformation at various locations and air temperature. The thermal dilation rate, shown in Fig. 24, ranges from −0.6–0.6 mm/℃. The velocity at the bridge towers is relatively low due to the deep pile foundations, which are less influenced by environmental factors and exhibit a weaker correlation with temperature. In contrast, the thermal dilation rate at the expansion joints and midspan is higher, indicating a stronger correlation with air temperature. Specifically, the thermal dilation rate at the midpoint is negatively correlated with air temperature, while the west and east expansion joints show positive and

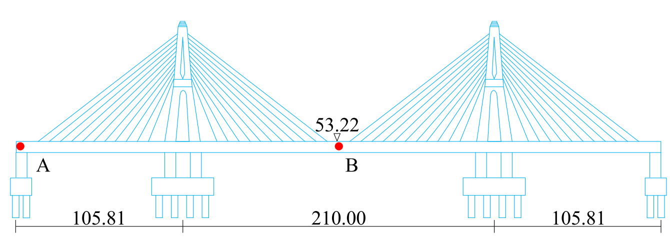

Fig. 22. Layout of the YPL Bridge (Unit: m).

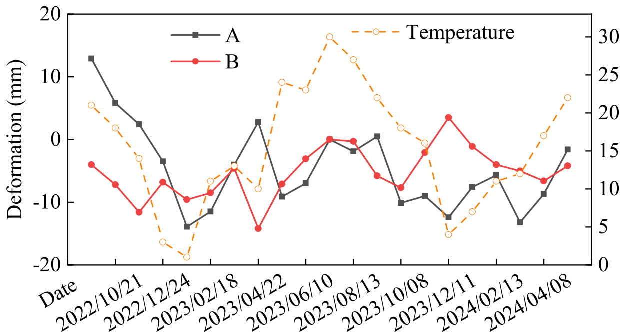

Fig. 23. Time-series LOS deformation of key points.

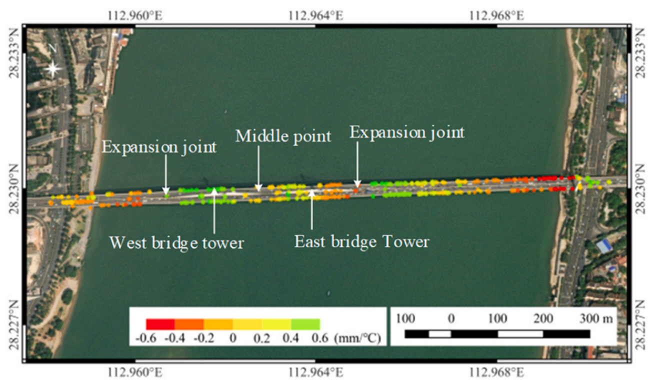

Fig. 24. LOS thermal dilation rate.

negative correlations, respectively. This is due to the thermal expansion of the main cable, which causes downward movement of the bridge deck as the temperature rises. Due to the constraints imposed by the bearings on vertical displacement at the expansion joints, the LOS deformation resulting from the thermal expansion and contraction of the box girder exhibits similar thermal dilation rates at the west and east expansion joints, but in opposite directions. Fig. 25 shows the deformation velocity, ranging from −10–8 mm/year. The deformation pattern follows a trend where the displacement is most pronounced at the midpoint, gradually decreases toward the bridge towers, and then increases again near the expansion joints on both the east and west sides of the bridge.

4.4. Verification of RDSI measurement precision

The basic principle of BDS positioning technology is to calculate the distance between the known position and the ground receiver by receiving the information sent by the satellite, position according to

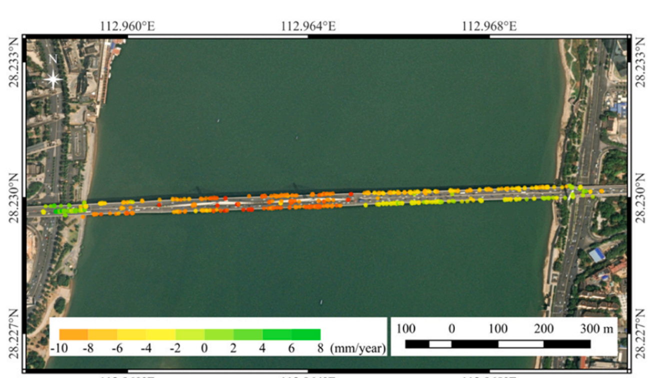

Fig. 25. LOS deformation velocity.

multiple satellite data, and obtain the spatial coordinates of the monitored point. The BDS' performance in deformation and vibration monitoring has been confirmed to be comparable with GPS [52,53]. Therefore, BDS was used to evaluate the performance of bridge monitoring through RDSI technique.

In this study, the BDS monitoring stations locate at points B and C on the SCJ Bridge, as marked with red dots in Fig. 17. The vertical, north-south, and east-west displacements of the bridge were measured by the BDS from March 22, 2024, to September 6, 2024 at a sampling interval of 30 minutes. The vertical displacement is derived from Eq. (16), and the longitudinal displacement of the bridge is calculated using Eq. (17), as presented in Fig. 26. The impact of transverse displacement on InSAR-measured LOS displacement is negligible due to the bridge's small width relative to its length. To analyze the displacement trends in different directions, univariate spline was applied to smooth temperature and displacement data. As shown in Fig. 26(a) and (b), longitudinal and vertical displacements exhibit a strong correlation with air temperature variations, with deformation increasing as temperature rises. In contrast, transverse displacement remains uniformly distributed along the longitudinal axis, consistent with previous studies [54]. The maximum longitudinal displacements at points B and C are 86.86 mm and 97.62 mm, respectively, while the corresponding vertical displacements reach 51.73 mm and 97.67 mm. As shown in Fig. 26(c), the peak transverse displacements at these points are 33.85 mm and 37.38 mm, respectively.

It is worth-noting that both BDS and InSAR provide relative displacement measurements. The BDS captures relative displacement from a stable reference station, while InSAR measures displacement from a high-coherence reference point. In addition, using a single SAR data source, the decomposition of LOS displacement into three directions based on SAR observation geometry may lead to overestimation or underestimation, depending on the projection direction of the bridge movement in the LOS direction. Therefore, the BDS-based LOS cumulative deformation was recovered to verify the precision of the RDSI method. Utilizing the BDS technique, the vertical, north-south, and east-west displacements of the bridge were recorded at the times of SAR image acquisition. These displacements were then combined in the LOS deformation calculation using Eq. (16). As presented in Table 2, the BDS-based LOS deformation is compared with the InSAR-derived LOS deformation. From April 8, 2024, to May 10, 2024, the movement directions calculated by both technologies are consistent, i.e., the positive and negative of the cumulative displacements were identical. The maximum discrepancy between the two methods is observed at point B, measuring only 1.18 mm, further validating the effectiveness of the refined DSI in thermal dilation phase estimation and RP selection for accurate deformation measurement.

5. Conclusion

This study explored the application of InSAR for deformation monitoring of bridge group. A refined DSI technique was proposed by incorporating improved thermal dilation estimation and RP selection, leading to reliable deformation measurements. The RDSI-measured deformation was validated against BDS data, confirming the precision of the proposed method. The main conclusions are as follows.

(1) Air temperature at bridge sites, derived from shared meteorological data through local thin-plate spline interpolation, improved thermal dilation estimation by incorporating spatial temperature variations. The discrepancy between theoretical calculations and InSAR-derived thermal dilation rates remains within 0.1 mm/°C at all longitudinal positions, except at $\Delta L = 420$ m, where the error ranges from 3.8 % to 13.33 %.

(2) A structure-knowledge-driven RP selection method was proposed to enhance the reliability of phase unwrapping. Using the conversion relationship between geographic and image coordinates,

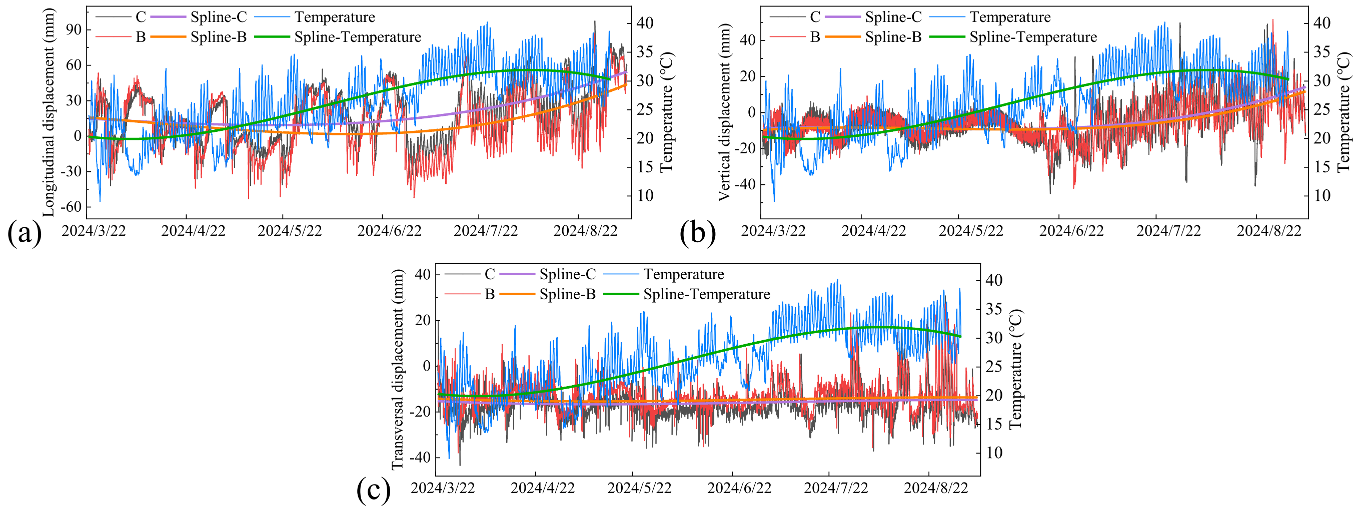

Fig. 26. Bridge displacement in different directions: (a) longitudinal, (b) vertical, (c) transverse.

Table 2
Comparison of cumulative LOS displacements measured by InSAR and BDS (Unit: mm).

Date	Position	D_n	D_e	D_v	α	β	θ	BD	RDSI	ΔBD vs. ΔRDSI
2024/4/8 6:15	C	43.5	3.46	−6.49	168.76°	31°	24.15°	−21.82	−5.6	0.28/0.1
2024/5/10 6:15		8.98	−17.64	−18.66				−22.10	−5.7	
2024/4/8 6:15	B	47.99	9.28	−4.60				−22.50	1.6	−6.29/−5.1
2024/5/10 6:15		1.61	−17.05	−15.47				−16.21	6.7	

the echo signal from the radar CR installed at the fixed bearing was identified as the RP. Additionally, an RP off the bridge and three RPs on the deck were selected for InSAR deformation comparison, which confirms the effectiveness of the structure-driven RP selection.

(3) The spatiotemporal deformation of bridges was analyzed using RDSI technique. Temporally, the LOS displacement exhibited an air temperature-dependent periodic behavior. Spatially, strong correlations between LOS deformation and air temperature were observed at the expansion joints, while the fixed bearing showed minimal movement.

(4) The LOS cumulative deformation was computed using vertical, north-south, and west-east displacements from BDS. A comparison between the calculated results and RDSI-measured results demonstrated consistent movement directions across different measurement points, with a maximum difference of 1.18 mm.

The performance of RDSI technique was well refined through structure-knowledge-driven RP and spatially interpolated air temperature, validating its feasibility for bridge group deformation monitoring. Further research is needed to determine RPs for bridges without artificial radar CRs, particularly in cases where the fixed bearing undergoes unnoticed movements due to scouring, settlements, or slow landslides. Additionally, the interpolation accuracy of air temperatures at bridge sites may be compromised in regions with sparse weather station coverage.

CRediT authorship contribution statement

Tan Zhongkun: Validation. **Yi Fan:** Validation. **Qin Xiaoqiong:** Investigation, Data curation. **Hao Guanwang:** Writing – original draft, Methodology. **Zhou Yun:** Supervision, Conceptualization.

Declaration of Competing Interest

The authors declare that they have no conflict of interest.

Acknowledgements

The authors sincerely appreciate the funding support provided by the National Natural Science Foundation of China (NSFC) (No.52278306), the Key Research and Development Program of Hunan Province (No. 2022SK2096), the Hunan Provincial Natural Science Foundation of China (No. 2023JJ70003), the National Natural Science Foundation of China (No. 52408327), the Natural Science Foundation of Hunan Province, China (No. 2024JJ6198).

Data availability

Data will be made available on request.

References

[1] Li Rong Z, Feng ZW, Wang GC, Hu QJ. J. Monitoring surface deformation over permafrost with an improved SBAS-InSAR algorithm: with emphasis on climatic factors modeling. Remote Sens Environ 2016;184:276–87.

[2] Infante Donato, Di Martire Diego, Confuorto Pierluigi, Tessitore Serena, Tòmas Roberto, Calcaterra Domenico, et al. Assessment of building behavior in slow-moving landslide-affected areas through DInSAR data and structural analysis. Eng Struct 2019;199:109638.

[3] Macchiarulo V, Milillo P, DeJong MJ, Gonzalez Mart J, Sánchez J, Giardina G. Integrated InSAR monitoring and structural assessment of tunnelling-induced building deformations. Struct Control Health Monit 2021;28(9):e2781.

[4] Ling C, Dollevoet R, Hanssen RF. Nationwide railway monitoring using satellite SAR Interferometry. IEEE J Sel Top Appl Earth Obs Remote Sens 2017;10(2): 596–604.

[5] Macchiarulo V, Milillo P, Blenkinsopp C, Giardina G. Monitoring deformations of infrastructure networks: a fully automated GIS integration and analysis of InSAR time-series. Struct Health Monit 2022;21(4):1849–78.

[6] Emadali L, Motagh M, Haghighi MH. Characterizing post-construction settlement of the Masjed-Soleyman embankment dam, Southwest Iran, using TerraSAR-X SpotLight radar imagery. Eng Struct 2017;143:261–73.

[7] Necula N, Niculiță M, Fiaschi S, Genevois R, Riccardi P, Floris M. Assessing urban landslide dynamics through Multi-Temporal InSAR techniques and slope numerical modeling. Remote Sens 2021;13(19):3862.
[8] Wu S, Yang Z, Ding X, Zhang B, Zhang L, Lu Z. Two decades of settlement of Hong Kong International Airport measured with multi-temporal InSAR. Remote Sens Environ 2021;248:111976.
[9] Huang QH, Crosetto M, Monserrat O, Crippa B. Displacement monitoring and modelling of a high-speed railway bridge using C-band Sentinel-1 data. Isprs J Photo Remote Sens 2017;128(1):204–11.
[10] Jung J, Kim DJ, Vadivel P, Yun SH. Long-term deflection monitoring for bridges Using X and C-Band Time-Series SAR Interferometry. Remote Sens 2019;11(11):1258.
[11] Cusson D, Rossi C, Ozkan IF. Early warning system for the detection of unexpected bridge displacements from radar satellite data. J Civ Struct Health Monit 2021;11(1):189–204.
[12] Ma P, Wu Z, Zhang Z, Au FT. SAR-Transformer-based decomposition and geophysical interpretation of InSAR time-series deformations for the Hong Kong-Zhuhai-Macao Bridge. Remote Sens Environ 2024;302:113962.
[13] Zhou Y, Hao GW, Chen J, Wei J, Zheng J. Long-term deformation monitoring of a steel-truss arch bridge using PSI technique refined by temperature field analysis. Eng Struct 2024;311:118164.
[14] Farneti E, Cavalagli N, Venanzi I, Salvatore W, Ubertini F. Residual service life prediction for bridges undergoing slow landslide-induced movements combining satellite radar interferometry and numerical collapse simulation. Eng Struct 2023;293:116628.
[15] Guzman-Acevedo GM, Vazquez-Becerra GE, Quintana-Rodriguez JA, Gaxiola-Camacho JR, Anaya-Diaz M, Mediano-Martinez JC, et al. Structural health monitoring and risk assessment of bridges integrating InSAR and a calibrated FE model. Struct 2024:106353.
[16] Qin XQ, Zhang L, Yang MS, Luo M, Liao MS, Ding XL. Mapping surface deformation and thermal dilation of arch bridges by structure-driven multi-temporal DInSAR analysis. Remote Sens Environ 2018;216:71–90.
[17] Qin X, Ding X, Liao M, Zhang L, Wang C. A bridge-tailored multi-temporal DInSAR approach for remote exploration of deformation characteristics and mechanisms of complexly structured bridges. ISPRS J Photo Remote Sens 2019;156:27–50.
[18] Li J, Xu Z, Zhang X, Ma W, He S. A persistent scatterer point selection method for deformation monitoring of under-construction cross-sea bridges using statistical theory and GMM-EM algorithm. Remote Sens 2024;16(12):2197.
[19] Hoppe EJ, Novali F, Rucci A, Fumagalli A, Del Conte S, Falorni G, et al. Deformation monitoring of posttensioned bridges using high-resolution satellite remote sensing. J Bridge Eng 2019;24(12):04019115.
[20] Liu Y, Yang H, Wang S, Xu L, Peng J. Monitoring and stability analysis of the deformation in the Woda landslide area in Tibet, China by the DS-InSAR method. Remote Sens 2022;14(3):532.
[21] Dong J, Liao M, Xu Q, Zhang L, Tang M, Gong J. Detection and displacement characterization of landslides using multi-temporal satellite SAR interferometry: a case study of Danba County in the Dadu River Basin. Eng Geol 2018;240:95–109.
[22] Zhang Z, Zeng Q, Jiao J. Deformations monitoring in complicated-surface areas by adaptive distributed Scatterer InSAR combined with land cover: taking the Jiaju landslide in Danba, China as an example. ISPRS J Photo Remote Sens 2022;186:102–22.
[23] Ma PF, Li T, Fang CY, Lin H. A tentative test for measuring the sub-millimeter settlement and uplift of a high-speed railway bridge using COSMO-SkyMed images. Isprs J Photo Remote Sens 2019;155:1–12.
[24] Herráez MA, Burton DR, Lalor MJ, Gdeisat MA. Fast two-dimensional phase-unwrapping algorithm based on sorting by reliability following a noncontinuous path. Appl Opt 2002;41:7437–44.
[25] Pritt MD. Phase unwrapping by means of multigrid techniques for interferometric SAR. IEEE Trans Geosci Remote Sens 1996;34:728–38.
[26] Zhou L, Yu H, Lan Y. Deep convolutional neural network-based robust phase gradient estimation for two-dimensional phase unwrapping using SAR interferograms. IEEE Trans Geosci Remote Sens 2020;58:4653–65.
[27] Vijay Kumar S, Sun X, Wang Z, Goldsbury R, Cheng I. A U-net approach for InSAR phase unwrapping and denoising. Remote Sens 2023;15(21):5081.
[28] Johnston PJ, Filmer MS, Fuhrmann T. Evaluation of methods for connecting InSAR to a terrestrial reference frame in the Latrobe Valley, Australia. J Geod 2021;95(10):115.
[29] Zhang B, Hestir E, Yunjun Z, Reiter ME, Viers JH, Schaffer-Smith D, et al. Automated reference points selection for InSAR time series analysis on segmented wetlands. IEEE Geosci Remote Sens Lett 2024;21:4008705.
[30] Mahapatra P, der Marel HV, van Leijen F, Samiei-Esfahany S, Klees R, Hanssen R. InSAR datum connection using GNSS-augmented radar transponders. J Geod 2018;92:21–32.
[31] Varugu BK, Jones CE, Wang K, Chen J, Osborne RL, Voyiadjis GZ. Optimized GNSS cal/val site selection for expanding InSAR viability in areas with low phase coherence: a case study for southern Louisiana. IEEE J Sel Top Appl Earth Obs Remote Sens 2024;17:4875–89.
[32] Xu YL, Chen B, Ng CL, Wong KY, Chan WY. Monitoring temperature effect on a long suspension bridge. Struct Control Hlth 2010;17(6):632–53.
[33] Zhou LR, Xia Y, Brownjohn JMW, Koo KY. Temperature analysis of a long-span suspension bridge based on field monitoring and numerical simulation. J Bridge Eng 2016;21(1):04015027.
[34] Xia Y, Chen B, Zhou XQ, Xu YL. Field monitoring and numerical analysis of Tsing Ma Suspension Bridge temperature behavior. Struct Control Hlth 2013;20(4):560–75.
[35] Xia Q, Wu WL, Li FN, Zhou XQ, Xu YL, Xia Y. Temperature behaviors of an arch bridge through integration of field monitoring and unified numerical simulation. Adv Struct Eng 2022;25(16):3492–509.
[36] Xia Q, Liu SL, Zhang J. Temperature analysis of a long-span suspension bridge based on a time-varying solar radiation model. Smart Struct Syst 2020;25(1):23–35.
[37] Zhou L, Liang C, Chen L, Xia Y. Numerical simulation method of thermal analysis for bridges without using field measurements. Procedia Eng 2017;210:240–5.
[38] Lorenz R, Petryna Y, Lubitz C, Lang O, Wegener V. Thermal deformation monitoring of a highway bridge: combined analysis of geodetic and satellite-based InSAR measurements with structural simulations. J Civ Struct Health Monit 2024;14:1237–55.
[39] Wang R, Zhang J, Liu X. A most-unfavorable-condition method for bridge-damage detection and analysis using PSP-inSAR. Remote Sens 2022;14(1):137.
[40] Selvakumaran S, Rossi C, Marinoni A, Webb G, Bennetts J, Barton E, et al. Combined InSAR and terrestrial structural monitoring of bridges. IEEE Trans Geosci Remote Sens 2020;58(10):7141–53.
[41] Guzman-Acevedo GM, Quintana-Rodriguez JA, Gaxiola-Camacho JR, Vazquez-Becerra GE, Torres-Moreno V, Monjardin-Quevedo JG. The structural reliability of the usumacinta bridge using InSAR time series of semi-static displacements. Infrastructures 2023;8(12):173.
[42] Ferretti A, Prati C, Rocca F. Permanent scatterers in SAR interferometry. IEEE Trans Geosci Remot Sen 2001;39(1):8–20.
[43] Hooper A, Bekaert D, Spaans K, Arikan M. Recent advances in SAR interferometry time series analysis for measuring crustal deformation. Tectonophysics 2012;514:1–13.
[44] Wahba G. Smoothing noisy data with spline functions. Numer Math 1975;24(5):383–93.
[45] Bates DM, Lindstrom MJ, Wahba G, Yandell BS. Gcvpack- routines for generalized cross validation. Commun Stat Simul Comput 1987;16(1):263–97.
[46] Cuervo-Robayo AP, Téllez-Valdés O, Gómez-Albores MA, Venegas-Barrera CS, Manjarrez J, Martínez-Meyer E. An update of high-resolution monthly climate surfaces for Mexico. Int J Clim 2014;34(7):2427–37.
[47] Goldstein RM, Zebker HA, Werner CL. Satellite radar interferometry: two-dimensional phase unwrapping. Radio Sci 1988;23:713–20.
[48] Ramberger G. Structural Bearings and Expansion Joints for Bridges. sixth ed. International Association for Bridge and Structural Engineering; 2002.
[49] American Institution of Steel Construction. Specification for structural steel buildings. 2022, ANSI/AISC 360-22.
[50] Zhao HW, Ding YL, Nagarajaiah S, Li AQ. Behavior analysis and early warning of girder deflections of a steel-truss arch railway bridge under the effects of temperature and trains: case study. J Bridge Eng 2019;24(1):05018013.
[51] Ding YL, Wang GX, Sun P, Wu LY, Yue Q. Long-term structural health monitoring system for a high-speed railway bridge structure. Sci World J 2015;2015:250562.
[52] Jiang W, Xi R, Chen H, Xiao Y. Accuracy analysis of continuous deformation monitoring using BeiDou navigation satellite system at middle and high latitudes in China. Adv Space Res 2017;59(3):843–57.
[53] Roberts GW, Tang X. The use of PSD analysis on BeiDou and GPS 10 Hz dynamic data for change detection. Adv Space Res 2017;59(11):2794–808.
[54] Shan Y, Li L, Xia Q, Gao W, Jing Q, Xia Y. Temperature behavior of cable-stayed bridges. Part I—global 3D temperature distribution by integrating heat-transfer analysis and field monitoring data. Adv Struct Eng 2023;26(9):1579–99.